

variation categories using the DNARates program [G. J. Olsen, S. Pracht, R. Overbeek, <http://geta.life.uiuc.edu/~gary/programs/DNARates.html> (1998)]. The Ti/Tv ratio for each of these second-round FASTDNAML analyses was estimated with PUZZLE using 16 gamma-distributed rate categories. The process of DNA rate categorization and tree inference was repeated until a stable tree topology was achieved. Data sets for ML bootstrapping were generated using the SEQBOOT program in PHYLIP [J. Felsenstein, *Cladistics* 5, 164 (1989)] and analyzed with FASTDNAML using the no-rates Ti/Tv ratio with global swapping across all nodes for each run. One hundred individual ML trees were obtained and used as input for DNARates and subsequent rounds of FASTDNAML, with the 16 gamma-rate Ti/Tv ratio. The resulting phylogenetic trees were compiled and analyzed using the CONSENSE program from PHYLIP. For protein analysis, we used an approximation to ML analysis: a heuristic search in PAUP* (with 10 random taxon-addition-order replicates and TBR branch-swapping) was based on a ML distance matrix calculated with PUZZLE. The distance matrix was generated using JTT substitution frequencies, amino acid usage estimated from the data, and site-to-site variation modeled on a gamma distribution with eight categories plus invariant sites and the shape parameter estimated from the data. Several different alignments and different masking of the conserved sequence regions were tested: No significant differences were found among the trees.

13. S.-M. Chaw *et al.*, *Proc. Natl. Acad. Sci. U.S.A.* **97**, 4086 (2000); Y. Van de Peer and R. De Wachter, *J. Mol. Evol.* **45**, 619 (1997).
14. P. J. Goodwin *et al.*, *Biochemistry* **37**, 10420 (1998).
15. J. Xiong, W. Fischer, K. Inoue, M. Nakahara, C. E. Bauer, data not shown.
16. Y.-L. Qiu *et al.*, *Nature* **402**, 404 (1999); J. P. Huelsenbeck, J. J. Bull, C. W. Cunningham, *Trends Ecol. Evol.* **11**, 152 (1996).
17. To generate a composite phylogenetic tree of all (bacterio)chlorophyll biosynthesis genes or gene products, all *bch/chl* (Bch/Chl) homologs shared among the bacterial and plant lineages (*bchl/chlI*, *bchD/chlD*, *bchH/chlH*, *bchl/chlL*, *bchN/chlN*, *bcbB/chlB*, and *bchG/chlG* for DNA sequences and Bch/ChlI, BchD/ChlD, BchH/ChlH, BchL/ChlL, BchN/ChlN, BcbB/ChlB, and BchG/ChlG for protein sequences) were also individually aligned and concatenated into a large data set containing 8504 positions in each nucleotide sequence (with the exclusion of the third codon position) and 3976 positions in each amino acid sequence. The combined data sets were used to infer phylogenetic trees. As shown in Fig. 1, there are three members in the *bchH* gene family in *C. tepidum*. Use of any one of the members in the calculation for the composite tree resulted in no difference in tree topology, though individual tree analysis showed different branching patterns for *bchH-1* (BchH-1) (Fig. 3B) relative to *bchH-2* (BchH-2) and *bchH-3* (BchH-3).
18. D. Moreira, H. L. Guyader, H. Philippe, *Nature* **405**, 69 (2000).
19. P. Beer-Romero, J. L. Favinger, H. Gest, *FEMS Microbiol. Lett.* **49**, 451 (1988).
20. S. Granick, in *Evolving Genes and Proteins*, V. Bryson and H. J. Vogel, Eds. (Academic Press, New York, 1965), pp. 67–68.
21. J. Xiong, K. Inoue, C. E. Bauer, *Proc. Natl. Acad. Sci. U.S.A.* **95**, 14881 (1998); D. H. Burke, J. E. Heast, A. Sidow, *Proc. Natl. Acad. Sci. U.S.A.* **90**, 7134 (1993).
22. R. E. Blankenship, *Photosynth. Res.* **33**, 91 (1992).
23. J. Xiong and C. E. Bauer, in preparation.
24. H. Ochman, J. G. Lawrence, E. A. Groisman, *Nature* **405**, 299 (2000); W. F. Doolittle, *Science* **284**, 2124 (1999).
25. Genomic DNA from *C. tepidum* (strain TLS, ATCC 49652) and *C. aurantiacus* (strain J10-fl) was isolated as previously described [A. Pospiech and B. Neumann, *Trends Genet.* **11**, 217 (1995)]. Photosynthesis genes from the two species were initially obtained through functional complementation of bacteriochlorophyll biosynthesis genes using pigment biosynthesis-deficient mutants of *Rhodospirillum rubrum*, as described [D. A. Young, C. E. Bauer, J. C. Williams, B. L. Marrs, *Mol. Gen. Genet.* **218**, 1 (1989)]. Three cosmids from *C. tepidum* (pCT4 for complementing *bchM⁻* strain, pCT6 for *bchF⁻*, and pCT8 for *bchG⁻*) and one cosmid from *C. aurantiacus* (pCA for *bchN⁻*) containing bacteriochlorophyll biosynthesis genes were obtained (Fig. 1). The cosmid inserts were subject to sequence analysis with the primer walking technique. DNA sequencing was performed with a fluorescent dye-labeled dideoxynucleotide sequencing reaction kit (Amersham) with an Applied Biosystems DNA sequencer (model 377, Perkin-Elmer). Oligonucleotide primers were synthesized by Operon Technologies. All of the DNA sequences we reported were determined completely on both strands. The flanking sequence of some of the cosmids was further extended by using inverse PCR according to the established protocol [H. Ochman, A. S. Gerber, D. L. Hartl, *Genetics* **120**, 621 (1988)]. The rest of the new photosynthesis gene sequences were initially obtained by PCR using degenerate primers based on alignments of the most highly conserved regions in homologous protein sequences. Inverse PCR was subsequently employed to obtain further flanking sequences. DNA sequences reported here have been annotated and deposited in GenBank with the following accession numbers: AF286047, AF287480, AF287481, AF287482, AY005135, AY005136, AY005137, AY005138, AF288458, AF288459, AF288460, AF288461, AF288462, and AF288602.
26. The obtained nucleotide sequence was analyzed with the Sequencher software (version 3.0, Gene Codes). Sequence compilation and ORF prediction and translation were performed with the aid of Sequencher and the GCG sequence analysis package (version 9.0). Homologous sequences were searched and retrieved from GenBank using BLAST [S. F. Altschul *et al.*, *Nucleic Acids Res.* **25**, 3389 (1997)] against a nonredundant protein database in GenBank. Multiple amino acid sequence alignments were generated with the aid of the computer program CLUSTALX (version 1.63b) and were further improved manually with the aid of SEQAPP (version 1.9) and SEQPUP (version 0.7) programs. The NH₂- or COOH-terminal overhangs and loops shared by <20% of the taxa as well as ambiguously aligned regions were excluded from further phylogenetic analysis. DNA sequences were aligned in frame according to the aligned corresponding amino acid sequences.
27. We thank Y. Fujita, D. Kehoe, H. Gest, S. Turner, and J. Palmer for critical discussions and comments during the preparation of the manuscript and M. Madigan for providing the *Chloroflexus aurantiacus* culture. Supported by NIH grant GM53940 (C.E.B.), an Arizona State University NASA astrobiology grant (C.E.B.), and a U.S.–Japan Cooperative Program on Photoconversion and Photosynthesis Research (K.I.).

29 December 1999; accepted 25 July 2000

REPORTS

Quantized Phonon Spectrum of Single-Wall Carbon Nanotubes

J. Hone,^{1*} B. Batlogg,² Z. Benes,³ A. T. Johnson,^{1†} J. E. Fischer³

The electronic spectra of carbon nanotubes and other nanoscale systems are quantized because of their small radii. Similar quantization in the phonon spectra has been difficult to observe because of the far smaller energy scale. We probed this regime by measuring the temperature-dependent specific heat of purified single-wall nanotubes. The data show direct evidence of one-dimensional quantized phonon subbands. Above 4 kelvin, they are in excellent agreement with model calculations of individual nanotubes and differ markedly from the specific heat of two-dimensional graphene or three-dimensional graphite. Detailed modeling yields an energy of 4.3 millielectron volts for the lowest quantized phonon subband and a tube-tube (or "lattice") Debye energy of 1.1 millielectron volts, implying a small intertube coupling in bundles.

The electronic structure of single-wall carbon nanotubes (SWNTs) has been extensively studied and is known to reflect confinement of electron waves to the one-dimensional (1D) molecular cylinder. How-

ever, the low-energy phonon structure of SWNTs is largely unexplored experimentally despite considerable theoretical work. The low-energy phonons are related to the mechanical properties and define the ther-

mal conductivity (1, 2), which will determine whether applications such as thermal management in molecular electronics are feasible. In addition, detailed knowledge of the phonon structure is important for understanding electron-phonon scattering in nanotubes (3, 4).

The phonon spectrum in SWNTs should display quantum size effects, whereby the two-dimensional (2D) phonon bands of graphene fold into a set of quantized 1D subbands, as is seen in the electronic band structure (5, 6). In reduced dimensions, the fundamental physics of phonon scattering

¹Department of Physics and Astronomy and Laboratory for Research on the Structure of Matter, University of Pennsylvania, Philadelphia, PA 19104–6272, USA. ²Bell Laboratories, Lucent Technologies, Murray Hill, NJ 07974, USA. ³Department of Materials Science and Engineering and Laboratory for Research on the Structure of Matter, University of Pennsylvania, Philadelphia, PA 19104–6272, USA.

*Present address: Department of Physics, California Institute of Technology, Pasadena, CA 91125, USA.

†To whom correspondence should be addressed.

(7, 8) and thermal equilibration is changed markedly. These basic issues, as well as potential applications such as highly sensitive bolometry, have driven continuing interest in low-dimensional phonon systems (8). Most experimental work in this field, such as the recent measurement of the quantum of thermal conductance (9), has used artificially designed nanostructures that are suspended to reduce thermal coupling to the substrate. In contrast to such structures, in which the 1D phonon regime has been difficult to access because of the small energy scale (10), carbon nanotubes are a molecular system whose small size and high stiffness result in a much larger energy splitting between 1D phonon subbands.

In SWNTs, the specific heat at constant pressure C_p is a direct probe of the phonon energy spectrum, the electronic contribution being negligible (11). In an ordinary three-dimensional (3D) solid, the low-temperature phonon $C_p(T)$ increases as T^3 . In an isolated nanotube, all of the circumferential degrees of freedom are frozen out at low temperature, so that the phonons are strictly 1D and $C_p(T)$ is linear in T (11, 12). However, in a bulk sample, strong phonon coupling between neighboring tubes will lead to 3D behavior and obscure the signature of 1D confinement. Because the phonon contribution to C_p is determined by the phonon (vibrational) density of states (PDOS) as a function of energy, we first examine the 1D PDOS of a SWNT and the effect of intertube coupling (Fig. 1) to set the stage for discussing our results.

The PDOS spectrum is shown for a 1.25-nm-diameter nanotube (the average diameter in available material) based on the phonon dispersion calculated by Saito *et al.* (13) (Fig. 1A). An isolated nanotube has a 1D phonon structure with four acoustic branches (one longitudinal, two transverse, and one torsional) with linear dispersions $E = \hbar v q$ (E is the phonon energy, \hbar is Planck's constant, v is the phonon velocity, and q is the wave vector) (14). The periodic boundary condition on the circumferential wave vector splits each of these modes into 1D "subbands" that translate into the sharp spikes, or 1D van Hove singularities, in the PDOS. The approximate location of the first optical ($E > 0$ at $q = 0$) subband is given by $E_{\text{sub}} \approx \hbar v/R$ (11), where R is the radius of the nanotube. It is clear why SWNTs are ideal for studying low-dimensional phonons: A small R and a large v (of order 10^4 m/s) lead to a measurably large subband splitting (larger nanotubes will have a smaller subband splitting and approach strictly 2D behavior as R increases). Detailed calculations for a 1.25-nm-diameter tube predict that the first subband edge is at $E_{\text{sub}} = 2.7$ meV, or 30 K.

In contrast to the 1D PDOS of the nanotube, the calculated PDOS of a single 2D graphene sheet (15) (Fig. 1A) varies smoothly, with no 1D singularities. It is greater in magnitude at $E = 0$ than that of the isolated tube, because a graphene sheet is weak to bending, whereas a tube is markedly stiffer. The acoustic "layer bending" mode in graphene has quadratic dispersion $E \propto q^2$ rather than the linear dispersion typical of acoustic modes in 3D solids. The quadratic dispersion yields a constant PDOS in 2D, which dominates the contribution of the other two (linear-dispersing) acoustic modes.

Because SWNTs are found in bundles ("ropes") of tens to hundreds of tubes, one must consider the effect of intertube coupling on the phonon structure and C_p . We first examine the analogous situation when graphene sheets are stacked to make 3D graphite. Coupling between adjacent graphene sheets introduces phonon dispersion in the c direction, shifting spectral weight from lower to higher energy states (Fig. 1). The characteristic energy for this process is the c -axis Debye energy near 12 meV. C_p of graphite shows a broad transition from 3D behavior below 12 meV (roughly 150 K) to 2D behavior above. A similar dimensional crossover should occur in SWNT ropes because of tube-tube coupling: The phonon structure of a rope will be 3D at low energy and reflect the structure of constituent tubes at higher energies. The characteristic energy of this crossover is the transverse Debye energy E_D^\perp .

A conceptual phase diagram (Fig. 1B) shows how the relation of E_D^\perp to E_{sub} will determine the conditions for dimensional crossover in a nanotube rope. In an isolated tube ($E_D^\perp = 0$), the phonons are 1D at the lowest temperatures: Only the four acoustic subbands are occupied. At a temperature $T_{1D} \approx E_{\text{sub}}/6k_B$ (5 K), where k_B is Boltzmann's constant, the first optical subband begins to contribute to the specific heat; well above T_{1D} , many subbands are occupied and the tube is essentially 2D. In a weakly coupled rope ($E_D^\perp < E_{\text{sub}}$), as the temperature increases from zero, the rope will go from a 3D coupled-tube regime to a 1D regime before crossing over to a 2D (multisubband) regime above T_{1D} . If, however, the tubes are strongly coupled ($E_D^\perp > E_{\text{sub}}$), then the transition will be from 3D directly to 2D, with no evidence of 1D quantization. Using a model based on the compression and shear behavior of graphite, Mizel *et al.* (16) calculated $E_D^\perp \sim 5$ meV (60 K), implying that SWNT ropes are in the strong-coupling regime.

We now turn to the experiment (17). SWNT samples were obtained from purified SWNT suspensions. Structural and

chemical analysis confirmed that the average tube diameter was 1.25 nm, that the tubes were found in crystalline bundles, and that a small amount (2 atomic %) of Ni/Co catalyst remained. The samples were protected from atmospheric contamination. Heat capacity was measured from 300 to 2 K with a relaxation technique. Two samples (9.5 and 2.5 mg) were measured with similar results, implying that there were no substantial systematic offsets in the measurement. The smaller mass causes the 2.5-mg data to have higher uncertainty, so we focus on the data from the 9.5-mg sample. The data presented below (Figs. 2, 3, and 4) have not been smoothed, so the spread in data points at a given temperature reflects

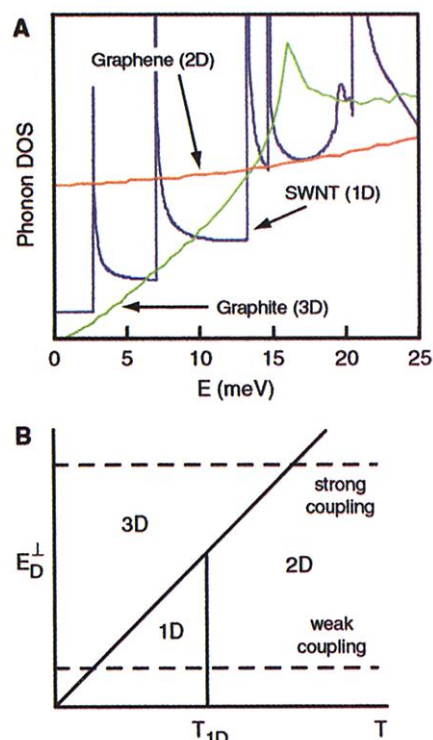


Fig. 1. (A) Theoretical phonon density of states (normalized per carbon atom) for 2D graphene (red) (13), 3D graphite (green) (15), and an isolated 1.25-nm-diameter SWNT (blue) (13). Interlayer coupling in graphite shifts spectral weight from lower to higher energies. (B) Conceptual phonon characteristic phase diagram for a SWNT rope. With increasing temperature, isolated tube phonons (zero coupling) cross over from a 1D regime where only acoustic subbands are occupied to a 2D regime as higher (optic) subbands are populated. This occurs at T_{1D} , which goes roughly as the inverse tube radius. In contrast, a bundle of weakly coupled tubes follows the lower dashed line: The phonons are 3D at low temperature, crossing over first to a 1D regime at a temperature that depends on the strength of intertube coupling, characterized by the transverse Debye energy E_D^\perp . If the coupling is strong (upper dashed line), the 1D regime is bypassed, and a quantized phonon spectrum is not observed in $C_p(T)$.

the measurement uncertainty, which is never more than a few percent.

The measured C_p , taken on slow cooling from 300 to 2 K, decreases monotonically with decreasing T , the lowest data point being 0.3 mJ/g-K at 2 K (Fig. 2, A and B, run 1). After run 1, the sample was left overnight at 4.2 K, and then measured on heating (Fig. 2B). The heat capacity from 2 to 20 K had increased dramatically, but this "excess" heat capacity disappeared above 20 K, consistent with adsorption of helium that had diffused into the vacuum space overnight. High-surface area carbons [including nanotubes (18)] are known to adsorb helium, and recent theoretical work (19) has predicted a high specific heat for helium adsorbed into the interstitial channels of a SWNT rope. As a check, the sample was warmed to 77 K, pumped out overnight, and then cooled quickly. The

fast-cooling data (run 2 in Fig. 2B) are identical to the slow-cooling data of run 1 and reflect the intrinsic specific heat of the sample.

The $C_p(T)$ curves calculated from the theoretical PDOS spectra are shown in Fig. 3. $C_p(T)$ directly reflects the dimensionality: At low temperature, an acoustic phonon mode in d dimensions with dispersion $E(q) \propto q^\alpha$ has $C_p \propto T^{d/\alpha}$. $C_p(T)$ of 2D graphene is dominated by the quadratic layer-bending mode and therefore has a roughly linear T dependence. In contrast, C_p for 3D graphite decreases more rapidly as T decreases below 80 K, a consequence of the 2D to 3D dimensionality crossover driven by interlayer coupling. Measurements on graphite (20) agree with the calculated phonon C_p down to 5 K, below which a small electronic contribution causes the measured data to lie slightly above the phonon curve. An isolated nanotube, with linear acoustic bands in 1D, will have $C_p \propto T$ at low T , with an increase in slope due to the contribution from the first subband above $T_{1D} \approx 5$ K. The nanotube curve lies well below the graphene one because the tube has no low-energy counterpart to the layer-bending modes. The C_p of a nanotube rope should follow the single-tube curve at high T and then show dimensional crossover to a stronger T dependence as T decreases. Compared with the analogous behavior in graphite ($E_D^c \approx 12$ meV),

strongly coupled ropes ($E_D^\perp = 5$ meV) should begin to deviate below the single-tube curve at ≈ 30 K. The calculated low- T C_p of a strongly coupled rope (16) (Fig. 3) shows a 3D behavior similar to that of graphite.

The measured specific heat (Fig. 3) is clearly largely consistent with the single-tube model, even though the sample consists mostly of large bundles. At intermediate temperatures (20 to 100 K), the data lie just above the single-tube prediction. We attribute this small discrepancy to 2 atomic % residual catalyst (21) (Fig. 3). Adding the catalyst contribution to the single-tube model fits the data quite well above 4 K. Below 4 K, the data lie substantially below the model curve, which we attribute to the crossover to 3D behavior on cooling. A crossover temperature near 4 K is much lower than predicted for strongly coupled tubes. Therefore, we conclude that the tubes are only weakly coupled, so that 1D quantum effects are observable.

Figure 4 emphasizes the low-temperature regime of 1D phonon confinement. The measured C_p increases linearly with T from 2 to 8 K, at which point the slope increases. This behavior is direct evidence

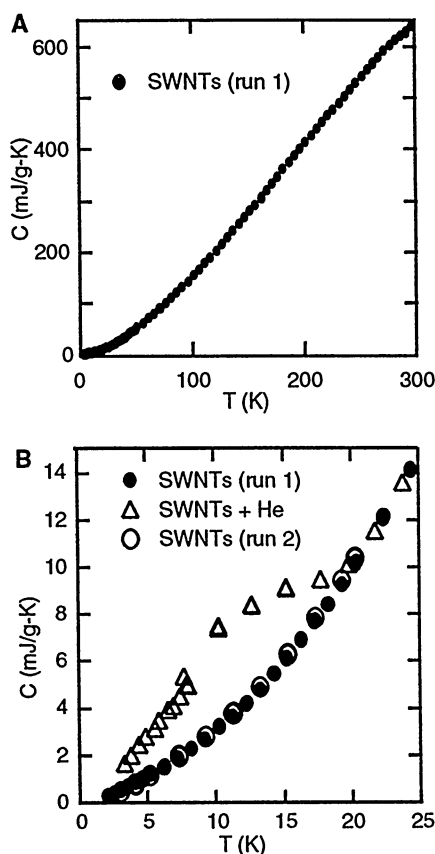


Fig. 2. (A) Specific heat of a sample consisting mainly of SWNT ropes, measured on first cooling from 300 to 2 K (run 1). (B) Low-temperature expansion of (A) (solid dots) and subsequent runs. Open triangles represent a heating run after leaving the sample at 4 K overnight, showing the effects of helium adsorption at 4 K and desorption at 20 K. Open circles (run 2) were recorded during rapid cooling after first warming to 77 K to completely desorb helium; these overlap perfectly with run 1, from which we conclude that helium adsorption is only an issue if the sample is held at 4 K for a long time.

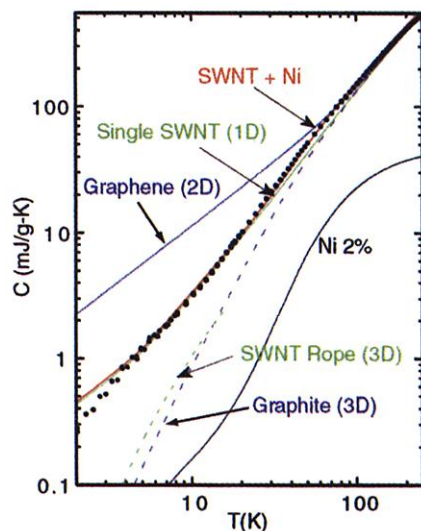


Fig. 3. Log-log plot of data (solid dots) compared with calculations for 2D graphene (solid blue), 3D graphite (dashed blue), isolated tubes (solid green), and strongly coupled ropes (dashed green). The data agree with the isolated tube model down to 5 K, indicating that tube-tube coupling is relatively weak. The agreement is improved at high T (solid red curve) by including the contribution of 2 atomic % nickel impurities (black curve). Below 5 K, the data fall substantially below the isolated tube prediction.

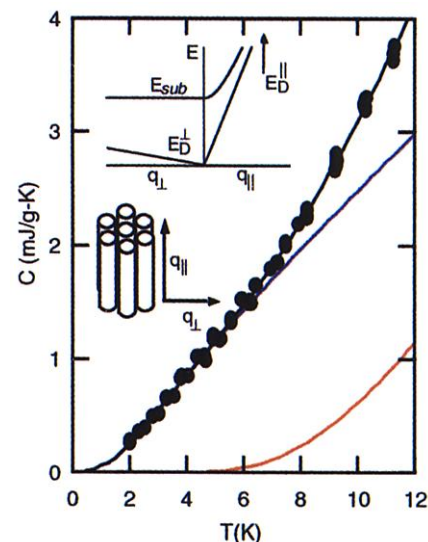


Fig. 4. Data on an expanded (linear) scale (solid dots) and a fit to an anisotropic two-band Debye model that accounts for weak coupling between SWNTs in a rope (black curve). The contribution from acoustic modes with large on-tube Debye energy E_D^\parallel and small transverse Debye energy E_D^\perp gives the blue curve, which fits the data at low temperatures but lies below the data above 8 K. Including the first 1D subband, approximated as a dispersionless optic branch at E_{sub} , adds a contribution given by the red curve. These are combined in the black curve, which fits the data over the entire range. Fitting parameters are given in the text; they imply that in real ropes the coupling and first subband threshold energies are smaller and larger, respectively, than previously believed.

for quantized 1D phonon subbands in nanotubes. However, C_p does not extrapolate linearly to zero at $T = 0$, as expected for isolated tubes. We know that the sample contains ropes, and we have evidence that intertube coupling is weak. An improved $C_p(T)$ model, accounting for both the quantized phonon subband structure of individual tubes and weak tube-tube coupling, can be derived from a simplified bundle phonon band structure (Fig. 4, inset). The four acoustic bands are combined into a single fourfold-degenerate band with longitudinal Debye energy E_D^{\parallel} and transverse Debye energy E_D^{\perp} . A doubly degenerate optical subband enters at E_{sub} with dispersion $E^2 = (\hbar v q_{\parallel})^2 + (E_{\text{sub}})^2$. Because $E_{\text{sub}} > E_D^{\perp}$, transverse dispersion of the subband can be ignored. The contribution from the acoustic band, with $E_D^{\parallel} = 92$ meV (1070 K) and $E_D^{\perp} = 1.2$ meV (14 K), displays roughly cubic temperature dependence below ~ 2 K, above which the intertube modes saturate and C_p displays the linear behavior characteristic of 1D phonons. The contribution from the first subband, with $E_{\text{sub}} = 4.2$ meV (50 K), is only substantial above 8 K. The total of the two contributions fits the data extremely well; deviation of $\sim 10\%$ in any of the fitting parameters resulted in a noticeably worse fit.

The experimental on-tube parameters derived from the fit can be compared with theory (13). The theoretical acoustic mode velocities translate into an effective Debye energy of 103 meV, slightly higher than our fitted 92 meV. Our fitted E_{sub} is larger than the theoretical single-tube value of 2.7 meV. These discrepancies may arise from intertube interactions whereby weak coupling modifies the elastic properties of the constituent tubes. For example, the first phonon subband (the low-energy mode with E_{2g} symmetry at $q = 0$) corresponds to tube flattening; this requires substantially more energy in a rope because tubes are constrained by their neighbors (22). The experimental tube-tube coupling, measured by $E_D^{\perp} = 1.2$ meV, is substantially smaller than the theoretical value of 5 meV (16). As a possible explanation, we note that Mizel *et al.* (16) base their model on coupling constants derived from graphite. However, the planes in graphite are identical, and the lattices of neighboring planes are commensurate. In contrast, neighboring tubes in a rope are most likely not identical. They will in general have different chiral angles (23) and diameters (24), so that the lattice structure on neighboring tubes will not be commensurate. This in turn implies a dramatic weakening of the corrugation in the intertube potential; tubes in a real rope may slide or twist more freely than expected from idealized models.

This observation of quantum size effects on the nanotube phonon spectrum and measurement of the above parameters have implications for applications and the theoretical understanding of nanotubes. The existence of quantized subbands in nanotubes indicates that theoretical and experimental work on low-dimensional phonons in artificial structures (25) is applicable to this technologically important material. The measured high on-tube Debye energy confirms, in a bulk sample, the high Young's modulus previously observed for individual tubes (26). The weak tube-tube coupling, however, implies that the mechanical strength of SWNT ropes will be relatively poor. It may be necessary to cross-link tubes within a rope or to separate them completely to realize their near-ideal properties in high-strength composites. On the other hand, weak coupling may be an advantage for high thermal conductivity. Berber *et al.* (2) find that strong tube-tube coupling decreases the high-temperature thermal conductivity of SWNT bundles by an order of magnitude relative to isolated tubes; weak coupling may imply no substantial reduction in the thermal conductivity when tubes are bundled into ropes. Similarly, in composites, the inner tubes in a rope should be relatively unperturbed by the surrounding matrix, which could also be an advantage for high thermal conductivity. The issues of commensurability that we raised as an explanation for the weak tube-tube mechanical coupling also suggest that there will be weak electronic coupling between neighboring SWNTs in a rope (25). Finally, our value for the first subband energy, large compared with single-tube force-constant theories, provides information about the effect of intertube interactions on single-tube deformation energies. An understanding of this effect is also critically important to obtain correct theoretical values for the energy of the radial breathing mode, commonly measured by Raman scattering to determine tube diameters and diameter distributions (22, 27, 28), and will have implications for the electronic overlap between neighboring tubes.

References and Notes

1. J. Hone, M. Whitney, C. Piskoti, A. Zettl, *Phys. Rev. B Cond. Matter* **59**, R2514 (1999).
2. S. Berber, Y. K. Kwon, D. Tomaneck, *Phys. Rev. Lett.* **84**, 4613 (2000).
3. C. L. Kane *et al.*, *Europhys. Lett.* **41**, 683 (1998).
4. Z. Yao, C. L. Kane, C. Dekker, *Phys. Rev. Lett.* **84**, 2941 (2000).
5. T. W. Odom, J. L. Huang, P. Kim, C. M. Lieber, *Nature* **391**, 62 (1998).
6. J. W. G. Wildoer, L. C. Venema, A. G. Rinzler, R. E. Smalley, C. Dekker, *Nature* **391**, 59 (1998).
7. R. E. Peierls, *Quantum Theory of Solids* (Clarendon, Oxford, 1955).
8. M. J. Kelly, *J. Phys. C Solid State Phys.* **15**, L969 (1982).
9. K. Schwab, E. A. Henriksen, J. M. Worlock, M. L. Roukes, *Nature* **404**, 974 (2000).

10. M. L. Roukes, *Physica B* **263**, 1 (1999).
11. L. X. Benedict, S. G. Louie, M. L. Cohen, *Solid State Commun.* **100**, 177 (1996).
12. The predicted electronic specific heat of a metallic nanotube is also linear in T but is two orders of magnitude smaller than the low- T linear phonon specific heat.
13. R. Saito, T. Takeya, T. Kimura, G. Dresselhaus, M. S. Dresselhaus, *Phys. Rev. B Cond. Matter* **57**, 4145 (1998).
14. In 3D materials, there must be three acoustic modes. When individual nanotubes are packed into a 3D crystalline structure, the torsional modes on neighboring tubes couple, rendering that mode optical.
15. R. Al Jishi, B. S. Elman, G. Dresselhaus, *Carbon* **20**, 127 (1982).
16. A. Mizel *et al.*, *Phys. Rev. B Cond. Matter* **60**, 3264 (1999).
17. Samples were synthesized by laser ablation in a 1100°C oven, with Ni and Co catalysts. The as-grown material was acid-treated to remove catalyst particles and amorphous carbon and was received as a water/surfactant suspension (cnstr.ice.edu/tubes/sem.html). This was then filtered, rinsed, dried, and tightly folded into two small (3 mm by 3 mm by 1 mm) pellets, which were vacuum-annealed at 1200°C. After annealing, the samples were analyzed by x-ray diffraction (XRD), high-resolution transmission electron microscopy (HRTEM), and energy-dispersive x-ray spectroscopy (EDX). The XRD showed peaks consistent with a crystalline hexagonal lattice; the position of the (1,0) peak gave an average tube diameter of 1.25 nm, consistent with TEM and XRD analysis of similar samples (25). HRTEM confirmed that the sample was composed of the usual large ropes of SWNTs. Finally, EDX revealed that the residual catalyst concentration was ≈ 2 atomic %. After analysis, the samples were baked at 300°C under dynamic vacuum for 3 days to remove atmospheric contaminants and kept under vacuum until minutes before the measurements were begun. Before the sample was loaded, a dab of Apiezon N grease was affixed to the cold stage, and the heat capacity of the addenda (stage plus grease) was measured over the entire temperature range (2 to 300 K) in a Quantum Design Physical Properties Measurement System. The sample was then removed from vacuum under an inert nitrogen atmosphere, weighed, placed onto the greased stage, and then loaded into the cryostat and evacuated. The total heat capacity of the stage and sample was then measured, and the previously measured heat capacity of the addenda was subtracted from the total heat capacity to give the data in Fig. 2.
18. W. Teizer, R. B. Hallock, E. Dujardin, T. W. Ebbesen, *Phys. Rev. Lett.* **82**, 5305 (1999).
19. M. W. Cole *et al.*, *Phys. Rev. Lett.* **84**, 3883 (2000).
20. M. G. Alexander, D. P. Goshorn, D. G. Onn, *Phys. Rev. B* **22**, 4535 (1980).
21. P. D. Desai, *Int. J. Thermophys.* **8**, 763 (1987).
22. D. Kahn and J. P. Lu, *Phys. Rev. B Cond. Matter* **60**, 6535 (1999).
23. L. Henrard, A. Loiseau, C. Journet, P. Bernier, *Eur. Phys. J. B* **13**, 661 (2000).
24. A. G. Rinzler *et al.*, *Appl. Phys. A Mat. Sci. Process.* **67**, 29 (1998).
25. A. A. Maarouf, C. L. Kane, E. J. Mele, *Phys. Rev. B* **61**, 11156 (2000).
26. M. M. J. Treacy, T. W. Ebbesen, J. M. Gibson, *Nature* **381**, 678 (1996).
27. L. Henrard, E. Hernandez, P. Bernier, A. Rubio, *Phys. Rev. B Cond. Matter* **60**, R8521 (1999).
28. A. M. Rao *et al.*, *Science* **275**, 187 (1997).
29. Supported by NSF grant DMR-9802560 (J.H. and A.T.J.), Department of Energy grant DEFG02-98ER45701 (J.H., Z.B., and J.E.F.), and NSF Materials Research Science Engineering Center grant DMR-9632598. We thank P. Papanek, D. E. Luzzi, and N. M. Nemes for the C_p calculation of graphite, HRTEM, and EDX analyses respectively; J.-P. Issi for bringing (20) to our attention; D. Colbert for graciously providing the SWNT material; and E. J. Mele, M. S. Dresselhaus, and A. Mizel for helpful conversations.

11 May 2000; accepted 18 July 2000